ADVANCED MATERIALS
www.advmat.de

Facet-Oriented Coupling Enables Fast and Sensitive Colloidal Quantum Dot Photodetectors

Margherita Biondi, Min-Jae Choi, Zhibo Wang, Mingyang Wei, Seungjin Lee, Hitarth Choubisa, Laxmi Kishore Sagar, Bin Sun, Se-Woong Baek, Bin Chen, Petar Todorović, Amin Morteza Najarian, Armin Sedighian Rasouli, Dae-Hyun Nam, Maral Vafaie, Yuguang C. Li, Koen Bertens, Sjoerd Hoogland, Oleksandr Voznyy, F. Pelayo García de Arquer, and Edward H. Sargent**

Charge carrier transport in colloidal quantum dot (CQD) solids is strongly influenced by coupling among CQDs. The shape of as-synthesized CQDs results in random orientational relationships among facets in CQD solids, and this limits the CQD coupling strength and the resultant performance of optoelectronic devices. Here, colloidal-phase reconstruction of CQD surfaces, which improves facet alignment in CQD solids, is reported. This strategy enables control over CQD faceting and allows demonstration of enhanced coupling in CQD solids. The approach utilizes post-synthetic resurfacing and unites surface passivation and colloidal stability with a propensity for dots to couple via (100):(100) facets, enabling increased hole mobility. Experimentally, the CQD solids exhibit a 10× increase in measured hole mobility compared to control CQD solids, and enable photodiodes (PDs) exhibiting 70% external quantum efficiency (vs 45% for control devices) and specific detectivity, $D^* > 10^{12}$ Jones, each at 1550 nm. The photodetectors feature a 7 ns response time for a 0.01 mm^2 area—the fastest reported for solution-processed short-wavelength infrared PDs.

1. Introduction

Colloidal quantum dots (CQDs) are building blocks for optoelectronics characterized by tunable optical and electronic properties.[1–12] Coupling of CQDs plays a crucial role in carrier transport: coupling along specific facets can enhance carrier mobility and diffusion length, opening the way to CQD solids that combine improved transport while still featuring excitonic photophysics.[13–18] Coupling strength is particularly important for large-size, low-bandgap CQDs: the decreased quantum confinement reduces wavefunction spill-out beyond the CQD boundaries, resulting in weaker CQD–CQD coupling and decrease in mobility by an order of magnitude for every 1 nm increase in CQD radius.[19]

CQD inks—dispersions of CQDs capped with short conductive ligands—have recently been employed in high-performing optoelectronic devices.[20,21] This is enabled by the combined effect of a high degree of surface passivation,[22] minimized energetic disorder,[20] and compatibility with scale-up techniques,[23] as opposed to CQDs passivated by solid-state ligand exchange. However, the reduced ligand length in CQD inks requires electrostatic colloidal stabilization, which complicates oriented assembly in CQD solids.[24–26] The lack of order and coupling in CQD solids limits efficient charge extraction, and thus curtails optoelectronic performance.

One way to improve coupling without hindering CQD passivation involves CQD shape modification. Improved coupling may in fact be achieved managing facet alignment by controlling the area ratio of the CQD facets, for example, by making one facet dominant and thus more prone to couple. However, this has not been attained in CQDs: the CQD facet ratio is determined by synthesis thermodynamics, wherein the total surface energy is minimized, thus also determining shape.[27,28] For lead sulfide (PbS) CQDs, the shape is close to spherical (or octahedral),[29] and this favors random coupling.

Here, we report ink-derived CQD solids showing enhanced coupling along a preferential direction. These show increased

M. Biondi, Prof. M.-J. Choi,[+] Dr. M. Wei, Dr. S. Lee, H. Choubisa, Dr. L. K. Sagar, Dr. B. Sun, Dr. B. Chen, P. Todorović, Dr. A. M. Najarian, A. Sedighian Rasouli, M. Vafaie, Prof. Y. C. Li, K. Bertens, Dr. S. Hoogland, Dr. F. P. García de Arquer, Prof. E. H. Sargent
Department of Electrical and Computer Engineering
University of Toronto
10 King's College Road, Toronto, Ontario M5S 3G4, Canada
E-mail: ted.sargent@utoronto.ca

Z. Wang, Prof. O. Voznyy
Department of Physical and Environmental Sciences
University of Toronto Scarborough
Scarborough, Ontario M1C 1A4, Canada
E-mail: o.voznyy@utoronto.ca

Prof. S.-W. Baek
Department of Chemical and Biological Engineering
Korea University
Seoul 02841, Republic of Korea

Prof. D.-H. Nam
Department of Energy Science and Engineering
Daegu Gyeongbuk Institute of Science and Technology (DGIST)
Daegu 42988, Republic of Korea

The ORCID identification number(s) for the author(s) of this article can be found under https://doi.org/10.1002/adma.202101056.

[+]Present address: Department of Chemical and Biochemical Engineering, Dongguk University, Seoul 04620, Republic of Korea

DOI: 10.1002/adma.202101056

hole transport properties and enable an advance in optoelectronic performance. The approach is enabled by colloidal-phase surface reconstruction of CQDs: we show that post-synthesis growth of CQDs allows us to override the thermodynamically driven shape. By manipulation of the CQD surface at the nanoscale, we control CQD shape, growing the facets along which coupling is more favorable for transport and facilitating coupling along these; while retaining quantum confinement and adequate CQD passivation. We obtain, as a result, CQD solids exhibiting a tenfold increase in hole mobility compared to controls.

The resulting CQD solids feature optimal coupling and passivation across thickness relevant to optoelectronic applications, leading to the demonstration of CQD photodiodes (PDs) that unite high external quantum efficiency (EQE = 70%) with high specific detectivity (D^* = 1.6 × 10^{12} Jones) at 1550 nm—a significant improvement over control PDs (EQE = 45% and D^* = 6 × 10^{11} Jones). The tenfold increase in hole mobility enables a temporal response of 7 ns for devices with an area of 0.01 mm^2, the fastest reported for solution-processed short-wavelength infrared (SWIR) PDs.

2. Results and Discussion

The shape of CQDs depends on their size and it changes from octahedral toward cubic as the diameter increases (**Figure 1**a).[28,29] CQDs of interest for infrared (IR) applications ($E_g \approx 0.8$ eV) are characterized by comparable levels of (100) and (111) facets. For PbS CQDs, the polar (111) facets are Pb-rich and readily passivated using ligands (iodide, in case of polar inks), while the non-polar (100) facets where Pb and S alternate are self-passivated and they are widely believed to be bare.[29–31]

In principle it is possible therefore for these CQDs to couple in three different ways: (100):(100) bare facets, (111):(111) passivated facets, and (100):(111) with only one layer of ligands in between.

We began by simulating using density functional theory (DFT) the effect of CQD orientation on coupling. CQD energy levels were brought into resonance with the aid of an external electric field. The external field is introduced to adjust for the inherent net polarization present due to the slight asymmetry of the two-dot system (see Experimental Section). At the anticrossing point, the splitting between the levels localized on two different CQDs is indicative of the electronic coupling strength (Figure 1b). The (100)–(100) orientation results in increased hole coupling and slightly decreased electron coupling compared to (111)–(111) (Figure 1c). The difference between the lattice of the (100) and (111) facets makes aligned (100)–(111) coupling difficult to achieve.

Preferential coupling along (100) is thus promising to achieve enhanced hole mobility. The (100) bare facets in fact promote epitaxially aligned fusion and thus stronger coupling. Indeed, in truncated-cubic CQDs where (100) facets are dominant and the coupling area is increased, we observed an overall increase in coupling,[18] and a fivefold increase for holes, in particular.

Simulations of CQD packing reveal how shape influences packing density. We observe increased packing density as the shape changes from truncated octahedron to truncated cube and cube. When the cubes are more truncated, the increased sphericity generates more disorder in the CQD orientation, causing mismatched (111)–(100) facets connections, while more cubic dots lead to the formation of domains of (100)–(100) connected CQDs (Figure S1, Supporting Information).

In light of these results, we postulated that the weak coupling and modest transport in state-of-art CQD solids fabricated from CQD inks may arise due to the broad facet distribution of IR CQDs, which can produce random orientation of CQDs in the final solid (Figure 1d).

We hypothesize that favoring (100):(100) coupling in the final film could improve transport by increasing hole mobility while maintaining good electron mobility.

We pursued therefore increased (100):(100) coupling by increasing the (100)/(111) ratio. We employed colloidal atomic layer deposition (c-ALD)[32–35] to reconstruct the CQD surface. c-ALD enables CQD growth at room temperature via the sequential addition of one monolayer of material per c-ALD cycle; the final CQDs can take on a shape that differs from the thermodynamically controlled synthetic shape.[32] During c-ALD, the different binding energies differ for specific facets: preferential binding to (111) facets will result in a fast growth along the (111) direction, resulting in an increase of (100) surface area and in anisotropic CQD growth.[32]

We obtained (100)-rich CQDs ($E_g \approx 0.83$ eV) by a c-ALD[33] sequential addition of S and Pb precursors to smaller as-synthesized CQDs. The growth procedure is depicted in **Figure 2**a and Figure S2, Supporting Information: oleic acid (OA)-capped CQDs and oleylamine are mixed in octane; an excess of ammonium sulfide in formamide (FA) is introduced as the S^{2-} source; and ammonium sulfide transfers to the octane phase by forming complexes with oleylamine.[32] Ammonium provides protons to strip off OA, while S binds preferentially to (111) facets.[28] After washing away the unreacted precursors, we add the Pb^{2+} source (Pb acetate) in FA; also easily transferred to the octane phase and known to bind strongly to S-rich (111).[36] We wash and redisperse the c-ALD CQDs in octane, obtaining a stable colloid; the stability is provided by the passivation with OA and Pb acetate, as shown by Fourier-transform infrared spectroscopy (FTIR) and nuclear magnetic resonance (NMR) spectroscopy (Figure S3, Supporting Information). For each cycle we observe a redshift in the position of the absorbance excitonic peak as expected with increasing CQD size, but, notably, the shift does not correspond to the growth of a full PbS monolayer (Figure 2b), in agreement with the hypothesized anisotropic CQD growth. Standard and c-ALD CQDs have a similar Stokes shift value, suggesting a comparable density of defects (Figure S4, Supporting Information).

We employed X-ray diffraction (XRD) on standard versus c-ALD CQDs to investigate further the difference in shape compared to standard CQDs (Figure 2c).[28] The intensity of the (111) and (200) XRD peaks is determined by the preferential alignment direction of the CQDs on the substrate. For standard CQDs the prevailing direction is [111], while it is [200] for the c-ALD CQDs; consistent with a preference of the c-ALD CQDs to align along the [200] direction. We hypothesize that this is caused by a higher presence of (200) diffracting planes, since the relative intensity of the (111) and (200) XRD peaks is determined by the preferential alignment direction of the CQDs on

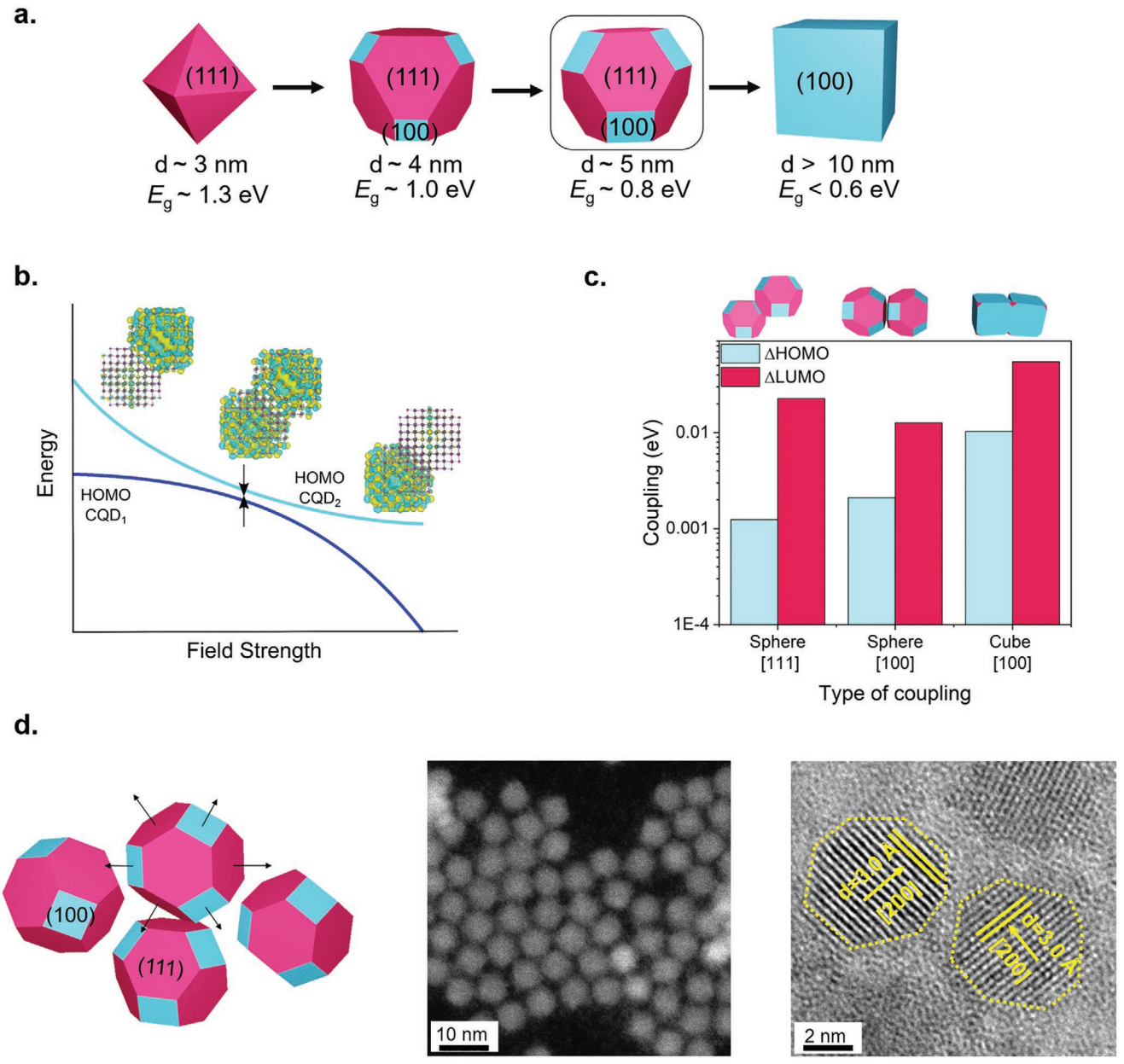

Figure 1. a) Shape variation of synthesized CQDs from octahedron to cube as a function of their diameter. As the size increases, the ratio (100)/(111) increases; for CQD with $E_g \approx 0.8$ eV (100)/(111) ratio is close to 1. b) HOMO levels of CQDs versus strength of the electric field applied. c) Coupling values for different types of coupling and CQD shape. d) IR CQDs where coupling is weak and not directional. The wide facet distribution determines a random arrangement of the CQD and weak coupling and STEM image of CQD solids, where CQD are randomly oriented.

the substrate. We simulated XRD patterns (see Experimental Section) as a function of the CQD shape: the simulations show a higher (111)/(200) in the case of a spherical CQD compared to a square CQD, agreeing with the observed dependence of the XRD pattern on the CQD shape (Figure S5, Supporting Information). While the absolute value of intensity could be influenced by the sample preparation method, XRD results represent an average over a large number of CQDs and can be an indirect evidence of increased (100) facets.

In order to better understand how the surface reconstruction induced by c-ALD modifies the shape of the CQDs, we performed transmission electron microscopy (TEM) on OA-capped CQDs before c-ALD, and after different numbers of c-ALD cycles (Figure 2d, and Figures S6–S12, Supporting Information).[37] We observe that, as the number of cycles increases, the fraction of (100) also increases. We compared the shape of standard CQDs and c-ALD CQDs (six c-ALD cycles) of similar diameter. We observe that c-ALD CQDs are indeed characterized by more (100) facets.

To quantify the difference in shape we compared, from TEM images, the (100)/CQD diameter ratio between standard and c-ALD CQDs (Figure 2e, details of the calculations in the

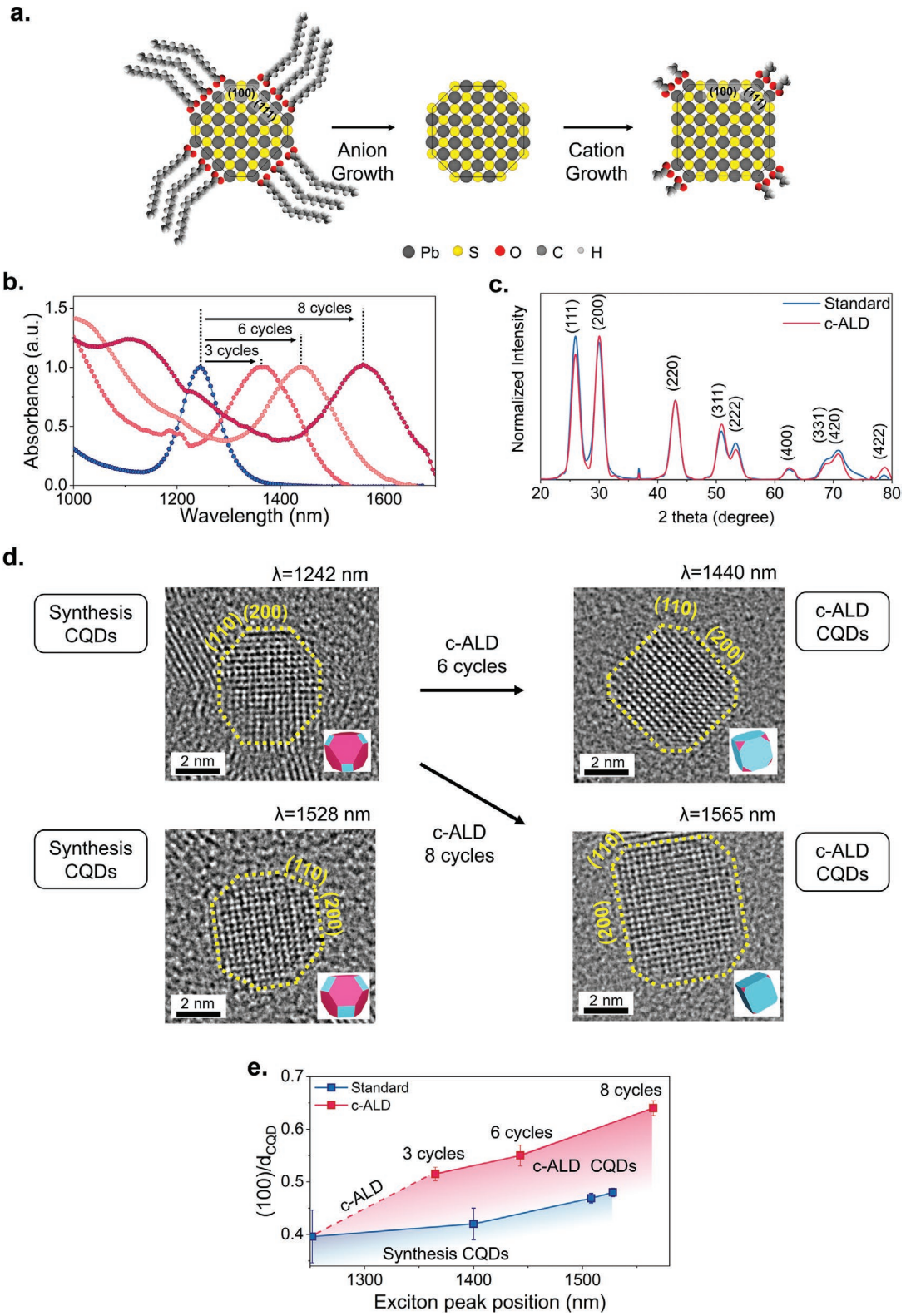

Figure 2. a) CQDs are grown to obtain (100) rich CQDs. Ammonium sulfide is added to OA-capped CQDs as S^{2-} source. S^{2-} binds to the (111) surface. Pb acetate is then added as source of Pb^{2+}, also binding to (111). b) Absorbance of CQDs before c-ALD and after a different number of c-ALD cycles. c) Experimental XRD measurements for standard and c-ALD CQDs. d) TEM images of CQDs before and after a different number of c-ALD cycles. e) Ratio of (100)/d_{CQD} determined from TEM images for different cycles of c-ALD and standard synthesized CQDs.

Experimental Section). The (100)/d_{CQD} ratio for a standard CQD with excitonic peak of ≈1520 nm is 0.48 ± 0.01, while it is 0.55 ± 0.02 for c-ALD CQDs of comparable diameter.

We then studied the characteristics of c-ALD CQD solids following exchange of the native insulating OA capping ligands to short conductive ligands, namely lead iodide and lead bromide (**Figure 3**a and Figure S13, Supporting Information).[20] STEM revealed bridging via the (100) surface (Figure 3a,b). We note that the CQD disposition differs from the standard CQD solid (Figure 1d): we observe partial CQD necking along (100) facets. CQD necking is feasible along bare (100) facets; the (111) facets are halide passivated, and thus are not expected to produce

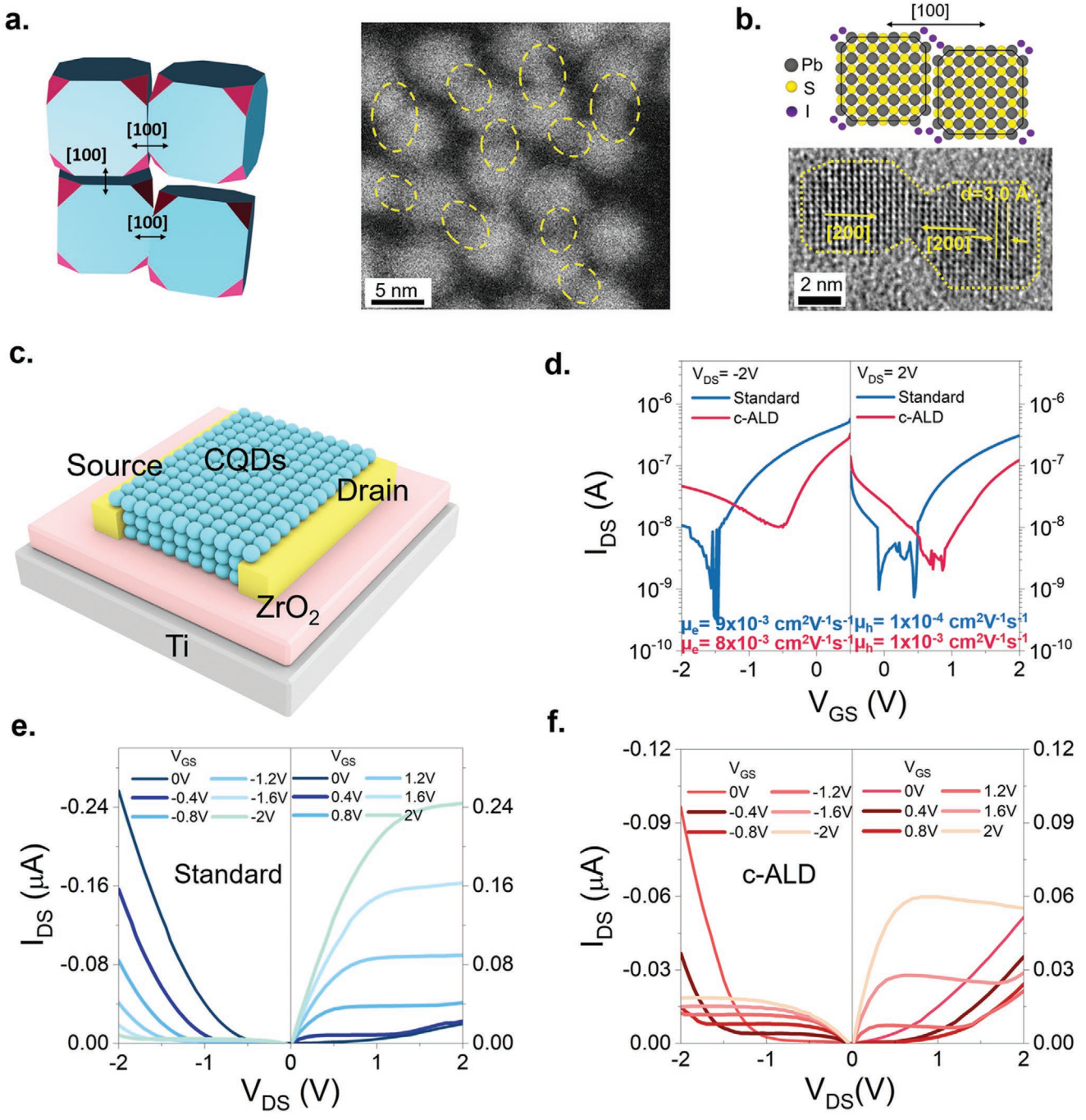

Figure 3. a) c-ALD CQDs after exchange, showing increased (100) coupling (left) and STEM image of c-ALD-exchanged CQDs. The (100) coupling is highlighted using yellow lines (right). b) TEM image of bridging between two CQDs; the lattice parameter reveals that the coupling direction is [200]. c) FET device. d) Transfer FET curves for standard and c-ALD CQD solids. e) I_{DS} versus V_{DS} curves at different V_{GS} for standard devices. f) I_{DS} versus V_{DS} curves at different V_{GS} for c-ALD devices.

necking. Figure 3b shows the magnification of partially connected CQDs: the lattice parameter reveals that the CQDs are coupled along the (100) facets.

The long-range disposition of c-ALD CQDs shows on average a higher interdot connectivity. The higher tendency of coupling along the (100) direction results in the arising of local-order zones showing partial cubic packing, while the standard films show hexagonal packing (Figure S13, Supporting Information).

We employed ultraviolet photoelectron spectroscopy (UPS) to determine the energy levels of the CQD solid after ligand exchange with halides. The bandgap was determined from the edge of the EQE spectrum, the Fermi level (E_F) and valence band maximum (VBM) from the UPS spectrum (Figure S14, Supporting Information), while the conduction band minimum was calculated from the VBM and E_g.[38] UPS shows more intrinsic character for the c-ALD samples, while the standard CQD films show n-type character with E_F 0.2 eV shallower than in the c-ALD sample. These results are consistent with a more cubic CQD, where the higher total amount of sulfur increases the difference between the vacuum level (E_{VAC}) and E_F.[39]

X-ray photoelectron spectroscopy (XPS) reveals that the chemistry of the final CQD solids after exchange with halides is similar for the standard and c-ALD samples (Figure S15, Supporting Information). We observe similar atomic ratio of iodide and bromide. The small decrease of halide content in the c-ALD samples is in agreement with the increased area of the (100) facets and therefore decrease halide-passivated facets.

To study the transport characteristics of c-ALD solids, we fabricated field effect transistors (FET). The measurements were carried out using a bottom-gate top-contact configuration (Ti gate/ZrO_2 gate dielectric/CQD solid [≈100 nm thickness]/Au source and drain) with a gate capacitance of 460 nF cm^{-2} (Figure 3c). We observe ambipolar transport in c-ALD solids and n-type dominant transport in the standard samples (Figure 3d–f). Mobilities were extracted from the transfer curves in saturation regime (Figure 3d, details of the calculations in the Experimental Section) for both standard and c-ALD CQD films: the electron mobility is comparable ($9 \times 10^{-3} \pm 1 \times 10^{-3}$ cm^2 V^{-1} s^{-1} for standard sample and $8 \times 10^{-3} \pm 5 \times 10^{-4}$ cm^2 V^{-1} s^{-1} for the c-ALD sample), while we observe a ten times increase in hole mobility for the c-ALD sample ($[1 \pm 0.3] \times 10^{-4}$ cm^2 V^{-1} s^{-1} for standard samples and $[1 \pm 0.3] \times 10^{-3}$ cm^2 V^{-1} s^{-1} for c-ALD samples). The decreased drain current in the saturation region of the output curves is attributed to electron traps.[40] This might be caused by the presence of OH groups on the ZrO_2 surface, which act as traps between the ZrO_2 and PbS active layer. Traps could also arise from partial necking occurring in c-ALD CQD solids, which might cause in-gap states.[41]

The increase of hole mobility compared to electron mobility agrees with DFT simulations. The studies reveal a picture of asymmetry between the hole and electron states in CQDs, and different degrees of confinement. In the case of PbS CQDs, conduction band states are formed from Pb 6p orbitals, while the valance band states are formed from S 3p orbitals. This induces a different degree of coupling depending on facets: the (111) PbS CQD surface is Pb-rich, as a result, coupling through (111)–(111) facet reinforces coupling of electron wavefunctions, while (100)–(100) coupling enhances hole coupling. More cubic CQDs are terminated by non-polar (100) facets and are overall less Pb-rich, endowing electrons and holes with similar degrees of access to the surface.

To determine the out of plane mobility in the same architecture as PDs, we measured space charge limited current (SCLC)—trap filling measurements on hole-only devices (ITO/MoO_3/CQDs/MoO_3/Ag, Figure S16, Supporting Information). We observe an 8× increased hole mobility for c-ALD devices, in agreement with FET measurements. In particular, as the number of c-ALD layers increases, mobility also increases ($\mu_h = 1.8 \times 10^{-4}$ cm^2 V^{-1} s^{-1} for two c-ALD cycles; $\mu_h = 3.9 \times 10^{-4}$ cm^2 V^{-1} s^{-1} for three c-ALD cycles; $\mu_h = 7.9 \times 10^{-4}$ cm^2 V^{-1} s^{-1} for six c-ALD cycles). We attribute this to enhanced coupling both in and out of plane, in agreement with an increase of coupling through (100) facets throughout the CQD solid.

We sought to use c-ALD CQD solids as the absorbing material in n–i–p IR PDs (cathode/electron transport layer/CQD active layer [≈250 nm thickness]/hole transport layer/anode, **Figure 4**a and Figure S17, Supporting Information).

c-ALD PDs show 73% EQE at the first excitonic peak, a significant improvement over the standard devices (45%, Figure 4b). We calculated the internal quantum efficiency (IQE, ratio of charges collected and photons absorbed in the device) of the devices to determine how efficiently the charges absorbed are extracted: the c-ALD devices show constant IQE, higher than 90% for all wavelengths (Figure 4c). Standard devices show a decreasing IQE and a drop to 70% at the excitonic peak. Under illumination, the c-ALD devices show a ×1.1 increase in fill factor and ×1.3 increase in J_{sc} as a consequence of improved transport (Figure S18, Supporting Information).

To investigate the sensitivity of the detector—its ability to detect signal above the noise—we obtained D^* from the measured noise equivalent power (NEP) (Figure S19, Supporting Information, details of the measurements and calculations in the Experimental Section) and observe improved D^* at 1 kHz for all wavelengths for the c-ALD sample (Figure 4d and Figure S20, Supporting Information). D^* reaches a value of 1.6×10^{12} Jones at 1550 nm. We also observe an improved shunt resistance from dark current measurement in the c-ALD samples compared to standard samples (Figure S21, Supporting Information), in agreement with a decreased NEP.

We used a 1540 nm laser source with a 150 fs pulse to determine the device fall time (τ, time taken by the signal to decrease from 90% to 10%, details of the measurements in the Experimental Section). The detector fall time is determined by charge carrier transit time and resistance capacitance constant, related to the device area.[42] We reduced the resistance capacitance effect on the temporal response by decreasing the PD active area. In small pixel area, carrier mobilities dominate τ (Figure S22, Supporting Information).

For 0.01 mm^2 devices, the fall time for the c-ALD device is 7 ns, while for standard devices it is 20 ns (Figure 4e). High mobility is a key enabler of fast PDs; we hypothesize that the slower response of standard CQD solids is attributed to the low hole mobility. The increase in detector speed is attributed to the increased coupling of c-ALD solids.

Mobility is proportional to CQD coupling:[14] transport in CQD solids happens through hopping of charges between

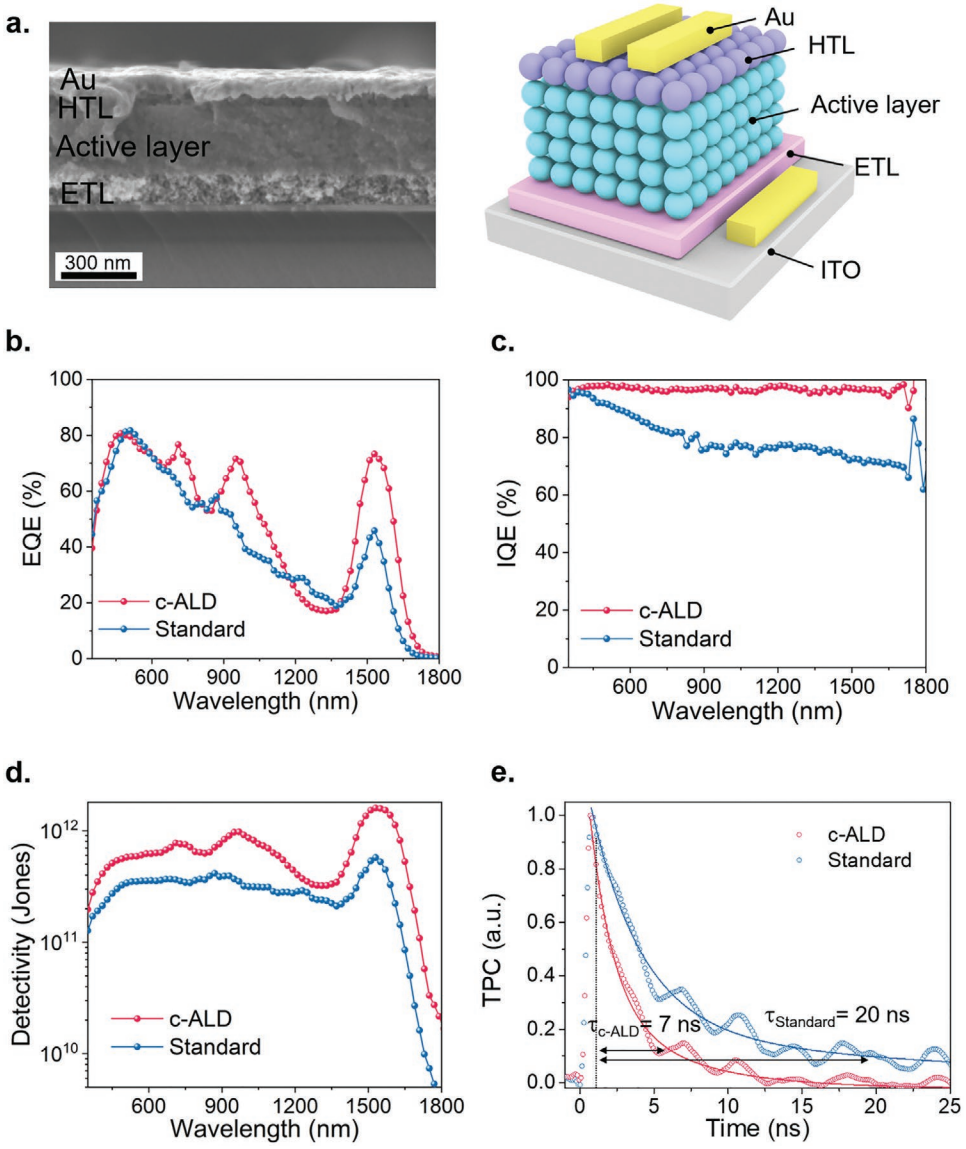

Figure 4. a) SEM cross section of a standard PD and representation of the device structure. b) Experimental EQE curve for a c-ALD and a standard device at 0 V. c) IQE for a c-ALD and standard device. d) Detectivity calculated from NEP measurements at 1 kHz for a c-ALD and standard device. e) Transient photocurrent (TPC) signal of a device for an active area of 0.01 mm^2 following excitation with a 1540 nm pulsed laser.

CQDs, and the coupling energy depends on the CQD distance (the tunnel barrier width) and the ligands around the CQDs (connected to the barrier height).[43] The increase in (100) facets enables increased coupling, as shown by DFT and mobility measurements, as it minimizes CQD distance and maximizes packing.

When the devices are subjected to 250 illumination cycles, the transient photocurrent measurement (TPC) does not show degradation (Figure S23, Supporting Information).

We studied the dependence of time response on the number of c-ALD cycles and observed an increase in speed as the number of cycles increased, in agreement with improved transport enabled by c-ALD reconstruction and enhanced coupling along the (100) facets (Figure S24, Supporting Information).

3. Conclusions

Coupling among CQDs is limited by hole mobility in state-of-art CQD solids based on inks, a fact that can be ascribed to weak CQD coupling arising due to the wide distribution of facets. The surface reconstruction method enables shape tuning and grows preferentially the (100) facets while keeping colloidal stability. The CQD solids obtained with the reconstructed CQDs show enhanced coupling and an increased hole mobility. The modified CQDs are used to fabricate SWIR PDs with high EQE, high D^*, and fast temporal response. Improved results can be achieved by enhancing the order of CQD coupling and employing techniques such as grazing-incidence small-angle scattering and grazing-incidence wide-angle scattering to explore more thoroughly the long-range packing in

the CQD solids. The same technique could be employed to further tune the shape of CQDs by changing the CQD precursors depending on their affinity with different facets. Finally, studies to further scale the c-ALD procedure will be essential for broad application of the materials technology. The applied advance is of interest especially as time-of-flight/LIDAR imaging for 3D scene acquisition enter the consumer electronics realm.

4. Experimental Section

Density Functional Theory Calculations: PbS CQDs were approximated with pairs of halide-capped (I) spherical or truncated cubic dots oriented to couple along the requisite planes. The computations were conducted using the CP2K software package[44–51] using the PBE/DZVP-MOLOPT-SR-GTH level of theory with GTH-PBE pseudopotentials.[52–55] The models were first optimized to minimize initial energies and to align the dots along their respective Miller planes. An external potential was then applied to the resulting aligned dots as single point computations and the HOMO wavefunctions were tracked in order to follow the transition of electron density from one dot to the other. The minimum gap between the low-lying LUMOs and upper HOMOs were collated to obtain the couplings between the dots.

Packing Density Simulations: The packing density was simulated using rigid body physics using the Blender animation suite.[56] Basic packing was constructed by dropping a number of cuboid structures representing the dots into a confined space. The cuboids were scattered before entering the bounding box in an effort to disrupt the arrangement before settling. Due to software constraints and the intended purpose of Blender being animation rather than nanoscale simulations, the default base unit scheme was used resulting in heavily upscaled representations (meters and kilograms). Dot representations were constructed from 2 by 2 by 2 unit cubes with corners truncated 0.5 units deep. For the spherical representation, the vertices were fully truncated (1 deep). Blender default rigid body system parameters were used leading to individual cuboids having a mass of 1 unit and friction was ignored. Facets were colored for visualization purposes and the representative dots were arrayed and dropped into 20 unit radii cylindrical containers using 800 cuboids. Packing was computed by taking a cross section of a layer of dots and comparing the space occupied with unoccupied space.

X-ray Diffraction Simulations: XRD patterns were simulated using the Atomic Simulation Environment (ASE) package's XrDebye module[57] using spheroid and cubic input geometries based on experimental structures available on the Materials Project database for cubic PbS.[58] Spherical dots were generated by truncation of a cubic supercell to the desired volume (4913 atoms for cubic and 4512 atoms for spherical).

Colloidal Quantum Dot Synthesis: OA-capped PbS CQDs were synthesized based on a previous report.[2] For the synthesis of CQDs with an excitonic peak at ≈1200 nm, 1.35 g of PbO, 4.5 mL of OA, and 15 mL of 1-octadecene were mixed in three-necked flask and degassed at 100 °C for 2 h to form a clear lead–oleate solution. Then, the flask was filled with N_2 and the temperature increased to 115 °C. 210 µL of bis(trimethylsilyl)sulfide (TMS) was dissolved in 8 mL of 1-octadecene in the glovebox and swiftly injected into the mixed solution. The color of the solution changed to brown and slowly cooled down to room temperature. The as-synthesized solution was moved to the glovebox and precipitated by adding acetone. This washing step was repeated thrice and the final CQD powder was dissolved in octane (50 mg mL^{-1}). The ratio of PbO, OA, and TMS was changed according to the desired final CQD size.

Colloidal Atomic Layer Deposition Procedure: The c-ALD procedure was modified from a previously reported procedure.[33] 3 mL of FA, 8 mL of octane, and 100 µL of oleylamine were mixed in a glass centrifuge tube. 1 mL of 40% ammonium sulfide solution in water was added to the FA phase and 1 mL of CQDs (50 mg mL^{-1}) was added to the octane phase. The tube was vortexed for 1 min. After separation of the two phases the FA was discarded and the octane phase was washed by adding 5 mL of FA and vortexing for 30 s (the washing step was repeated twice). In order to ease the phase separation, the glass tubes were centrifuged for 5 s when needed. The FA phase was discarded and 3 mL of fresh FA was added. 0.1 M solution of Pb acetate dissolved in FA was then added to the FA in the glass tube. The glass tube was vortexed for 1 min and FA was discarded. The washing procedure was repeated twice as before. The procedure was repeated for as many times as needed to achieve the desired absorption wavelength depending on the size of the starting dots. After growth, 50 µL of lead oleate was added to the CQDs; next an excess of acetone was added and the dots were centrifuged at 7000 rpm for 10 min and redispersed in 1 mL of octane. The washing procedure was repeated twice and the CQDs were stored in a N_2 filled glovebox.

Colloidal Quantum Dot Photodiode Fabrication: The ZnO nanoparticles were synthesized using a published method.[11] The ZnO nanoparticles were spin-cast on ITO substrate at 5000 rpm (83 × [2π] rad s^{-1}) for 20 s (2 layers, ≈150 nm thickness). The CQDs were exchanged using an existing procedure.[20] The CQD films were spin-cast on the ZnO/ITO substrate with a concentration of 260 mg mL^{-1} of CQD inks in butylamine and dimethylformamide (4:1) with dynamic spinning (step 1 = 800 rpm; step2 = 1000 rpm) and annealed at 70 °C for 10 min in a N_2-filled glovebox (≈200 nm thickness). For the fabrication of the HTL, the OA-capped CQDs were spin-cast (2500 rpm [42 × [2π] rad s^{-1}] for 10 s) and soaked with a 0.01 vol % EDT solution in ethyl acetate for 30 s and followed by washing thrice with ethyl acetate; the procedure was repeated twice (≈60 nm thickness). A 120 nm Au top electrode was deposited by e-beam evaporation.

Colloidal Quantum Dot Ligand Exchange: The exchange was based on a previously published procedure.[20] Lead halides (lead iodide 0.1 M and lead bromide 0.02 M) and NH_4Ac (0.04 M) were predissolved in dimethylformamide to form the ligand exchange solution. 10 mL of ligand exchange solution were added in a centrifuge tube; then 10 mL of octane was added. 1.4 mL of CQDs (50 mg mL^{-1}) was then added to the octane phase and the solution was vortexed for 90 s. The CQDs transfer to the DMF solvent and the supernatant was discarded. Fresh octane (10 mL) was added to remove excess OA ligands and the tube was vortexed for 30 s. The washing step was repeated thrice. Then, the CQDs were transferred in glass tubes (5 mL per tube) and 3 mL of toluene was added to precipitate the dots after 2 min of centrifugation. The CQDs were dried for 10 min and redispersed in a 4:1 BTA:DMF solution (260 mg mL^{-1}) to form a stable CQD ink. The 4:1 BTA:DMF ratio was needed to obtain good stability for CQDs with $d > 5$ nm.

Dark Current and External Quantum Efficiency Measurement: Current–voltage characteristics were measured with a Keithley 2400 source measuring in dark conditions. Devices were tested under a continuous nitrogen flow. The *I–V* curves were scanned from –1.0 to +1.0 V at 0.02 V interval steps. EQE spectra were taken by subjecting the devices to chopped (220 Hz) monochromatic illumination (400 W Xe lamp passing through a monochromator and appropriate cutoff filters). The power of the incident light is reported in Figure S20, Supporting Information. Newport 818-UV and Newport 838-IR photodetectors were used to calibrate the output power. The response of the device was measured with a Lakeshore preamplifier feeding into a Stanford Research 830 lock-in amplifier at short-circuit conditions.

Internal Quantum Efficiency Calculation: The IQE values were calculated dividing the EQE at 0 V and biased EQE at (–1 V).[59]

Fourier-Transform Infrared Spectroscopy Measurements: FTIR spectra were obtained using a Thermo Scientific iS50 Spectral range 4000–1000 cm^{-1} with an ATR accessory. Samples were prepared on glass substrates.

Nuclear Magnetic Resonance Measurements: The ^{1}H NMR resonance signal was collected with a 600 MHz Agilent DD2 NMR spectrometer. CQD samples were prepared by adding 500 µL of the stable colloid solution with 100 µL of deuterated toluene as the lock solvent.

Transmission Electron Microscopy Measurements: TEM samples of exchanged-CQDs were prepared by spin-coating CQD solution on a carbon-coated Cu grid and measured on Hitachi H3300F at 300 kV. TEM samples of OA-capped CQDs were prepared by dropping a

CQD solution (5 mg mL^{-1} in octane) on a carbon-coated Cu grid and measured on Hitachi H3300F at 300 kV.

(100)/d_{CQD} Ratio Measurements: The ratio was determined by measuring the length of (100) facet from TEM images when looking at the [100] direction and the CQD diameter. The length was measured using Gatan software. The error bars were obtained from ten measurements.

X-ray Diffraction Measurements: CQD films were fabricated by drop-casting on glass substrates. The measurements were carried on using a Rigaku MiniFlex 600 diffractometer using a monochromatized copper Kα radiation ($\lambda = 1.5406$ Å).

Field-Effect Transistors' Fabrication and Measurements: Bottom-gate top-contact FET configuration was used as follows: 70 nm of titanium gate was thermally evaporated onto a glass substrate, followed by 15 nm of ZrO_2 ($\varepsilon = 10$) as a dielectric layer using atomic layer deposition. The substrates were backed at 300 °C for 1 h in a N_2 filled glovebox. The QDs were exchanged with lead halides following the same procedure employed for the fabrication of PDs. The CQD inks dissolved in BTA and DMF were spin-coated onto the substrates. Then 70 nm of Au source/drain electrodes were thermally deposited using an Angstrom Engineering Amod deposition system. Agilent 4155 semiconductor analyzer was used to characterize the FET devices.

Carrier mobility of FET devices was calculated using the Equation (1) as follows when $V_{DS} > (V_{gs} - V_{Th,e})$ for electron mobility and $V_{DS} > (V_{gs} - V_{Th,h})$ for hole mobility:[60]

$$I_{DS} = \mu C_i (V_{gs} - V_{th})^2 W/2L \tag{1}$$

where V_{DS} was the source–drain voltage, I_{DS} was the drain current, μ was the carrier mobility in the linear regime, C_i was the gate dielectric capacitance per unit area (450 nF cm^{-2}), V_{gs} was the gate voltage, V_{th} was the threshold voltage, L was the channel length (50 µm), and W was the channel width (2500 µm).

The thickness of the FET samples was around 100 nm.

Space-Charge-Limited Current Measurements: *J–V* characteristics of hole only devices (ITO/MoO_3/CQDs/MoO_3/Ag) were measured; the thickness of the CQD layer was 200–300 nm. The equation below was used to calculate the mobility in the SCLC regime following Mott–Gurney's law ($J \sim V^2$):

$$J_{SCLC} = \frac{9}{8}\varepsilon_0 \varepsilon_r \mu_{SCLC} \frac{V^2}{L^3} \tag{2}$$

where ε_0 (8.854 × 10^{-12} F m^{-1}) and ε_r were the vacuum and relative dielectric permittivities, V was the applied voltage, and L was the film thickness. A value of 18.0 was used for relative dielectric permittivity of PbS CQD films.[61]

Ultraviolet Photoelectron Spectroscopy Measurements: UPS measurements were carried out on CQD solids after ligand exchange with halides. A helium discharge source (HeI α, $h\nu = 21.22$ eV) was used and the samples were kept at a take-off angle of 88°. During measurement, the sample was held at a –15 V bias relative to the spectrometer in order to efficiently collect low kinetic-energy electrons. E_F was calculated from the equation: $E_F = 21.22$ eV − SEC, where SEC was the secondary electron cut-off. The difference between valence band and E_F, was determined from the valence band onset in the valence band region.

X-ray Photoelectron Spectroscopy Measurements: XPS measurements were carried out on CQD solids after ligand exchange with halides. XPS measurements were carried out using a Thermo Scientific K-Alpha system, with a 75 eV pass energy, and binding energy steps of 0.05 eV.

Noise Equivalent Power Measurement and Specific Detectivity Calculation: The average noise current was measured using multiple readings from a SR830 lock-in using its noise measurement system. The detector was connected with a low-noise SR570 preamplifier to the lock-in. All measurements were performed in a dark, shielded enclosure at room temperature (295 K) under nitrogen flow at 1 kHz frequency.

Noise current (I_N) was determined through the following formula:

$$I_N = V_N \times S \tag{3}$$

where V_N was the voltage noise readout from the SR830 in V Hz$^{-1/2}$ and S was the sensitivity of the transimpedance amplifier—in this case, 10 nA V^{-1}.

For c-ALD, $I_N = 1.7 \times 10^{-13}$ A Hz$^{-1/2}$.

For Standard, $I_N = 2.9 \times 10^{-13}$ A Hz$^{-1/2}$.

The EQE spectrum was used to calculate responsivity (R):

$$R = \frac{\text{EQE}\cdot\lambda}{1240} \tag{4}$$

where λ is the wavelength.

$R = 0.9$ A W^{-1} at the excitonic peak for c-ALD sample

The NEP at the excitonic peak is given by:

$$\text{NEP} = \frac{I_N}{R} \tag{5}$$

c-ALD NEP = 1.7×10^{-13} W Hz$^{-1/2}$.

Standard NEP = 3.0×10^{-13} W Hz$^{-1/2}$.

Finally, detectivity at each wavelength was determined through the formula:

$$D^* = \frac{R\sqrt{A}}{I_N} \tag{6}$$

where A was the device electrical area (0.09 cm^2).

Transient Photocurrent Measurement: TPC measurements were performed under air ambient. Femtosecond pulses (1030 nm, 5 kHz repetition rate) were generated by a Yb:KGW laser (Pharos, Light Conversion), passed through an optical parametric amplifier (Orpheus, Light Conversion), and selected for 1540 nm wavelength. The signals were recorded using an oscilloscope with an input impedance of 50 Ω. For stability measurements, a 940 nm diode laser controlled by a function generator to produce square pulses with frequency and pulse width of 2.5 KHz and 40 ns, respectively, was used. The transient photoresponse of the devices (pixel size of 0.09 cm^2) was recorded using the oscilloscope (no external bias, 50 Ω impedance)

Supporting Information

Supporting Information is available from the Wiley Online Library or from the author.

Acknowledgements

M.B., M.-J.C., and Z.W. contributed equally to this work. This work was supported by the Natural Sciences and Engineering Research Council (NSERC) of Canada. Computations were performed on the Niagara supercomputer at the SciNet HPC Consortium. SciNet was funded by: the Canada Foundation for Innovation; the Government of Ontario; Ontario Research Fund – Research Excellence; and the University of Toronto. The authors thank D. Kopilovic, E. Palmiano, L. Levina, and R. Wolowiec for the technical support.

Conflict of Interest

The authors declare no conflict of interest.

Data Availability Statement

The data that support the findings of this study are available from the corresponding author upon reasonable request.

Keywords

colloidal atomic layer deposition, colloidal quantum dots, coupling, facets, photodetectors

Received: February 7, 2021
Revised: April 14, 2021
Published online:

[1] I. Moreels, K. Lambert, D. Smeets, D. De Muynck, T. Nollet, J. C. Martins, F. Vanhaecke, A. Vantomme, C. Delerue, G. Allan, Z. Hens, *ACS Nano* **2009**, *3*, 3023.
[2] M. A. Hines, G. D. Scholes, *Adv. Mater.* **2003**, *15*, 1844.
[3] M. V. Kovalenko, L. Manna, A. Cabot, Z. Hens, D. V. Talapin, C. R. Kagan, V. I. Klimov, A. L. Rogach, P. Reiss, D. J. Milliron, P. Guyot-Sionnnest, G. Konstantatos, W. J. Parak, T. Hyeon, B. A. Korgel, C. B. Murray, W. Heiss, *ACS Nano* **2015**, *9*, 1012.
[4] J. M. Pietryga, Y. S. Park, J. Lim, A. F. Fidler, W. K. Bae, S. Brovelli, V. I. Klimov, *Chem. Rev.* **2016**, *116*, 10513.
[5] Y. Shirasaki, G. J. Supran, M. G. Bawendi, V. Bulović, *Nat. Photonics* **2013**, *7*, 13.
[6] Y. Wang, Z. Liu, N. Huo, F. Li, M. Gu, X. Ling, Y. Zhang, K. Lu, L. Han, H. Fang, A. G. Shulga, Y. Xue, S. Zhou, F. Yang, X. Tang, J. Zheng, M. A. Loi, G. Konstantatos, W. Ma, *Nat. Commun.* **2019**, *10*, 5136.
[7] J. P. Clifford, G. Konstantatos, K. W. Johnston, S. Hoogland, L. Levina, E. H. Sargent, *Nat. Nanotechnol.* **2009**, *4*, 40.
[8] M. J. Choi, F. P. García de Arquer, A. H. Proppe, A. Seifitokaldani, J. Choi, J. Kim, S. W. Baek, M. Liu, B. Sun, M. Biondi, B. Scheffel, G. Walters, D. H. Nam, J. W. Jo, O. Ouellette, O. Voznyy, S. Hoogland, S. O. Kelley, Y. S. Jung, E. H. Sargent, *Nat. Commun.* **2020**, *11*, 103.
[9] J. Gao, S. C. Nguyen, N. D. Bronstein, A. P. Alivisatos, *ACS Photonics* **2016**, *3*, 1217.
[10] F. Prins, M. Buscema, J. S. Seldenthuis, S. Etaki, G. Buchs, M. Barkelid, V. Zwiller, Y. Gao, A. J. Houtepen, L. D. A. Siebbeles, H. S. J. Van Der Zant, *Nano Lett.* **2012**, *12*, 5740.
[11] J. Lim, Y. S. Park, V. I. Klimov, *Nat. Mater.* **2018**, *17*, 42.
[12] I. Moreels, Y. Justo, B. De Geyter, K. Haustraete, J. C. Martins, Z. Hens, *ACS Nano* **2011**, *5*, 2004.
[13] N. Yazdani, S. Andermatt, M. Yarema, V. Farto, M. H. Bani-hashemian, S. Volk, W. M. M. Lin, M. Luisier, V. Wood, *Nat. Commun.* **2020**, *11*, 2852.
[14] A. P. Kaushik, B. Lukose, P. Clancy, *ACS Nano* **2014**, *8*, 2302.
[15] Y. Liu, N. Peard, J. C. Grossman, *J. Phys. Chem. Lett.* **2019**, *10*, 3756.
[16] C. R. Kagan, C. B. Murray, *Nat. Nanotechnol.* **2015**, *10*, 1013.
[17] N. Yazdani, D. Bozyigit, K. Vuttivorakulchai, M. Luisier, I. Infante, V. Wood, *Nano Lett.* **2018**, *18*, 2233.
[18] P. Liljeroth, K. Overgaag, A. Urbieta, B. Grandider, S. G. Hickey, D. Vanmaekelbergh, *Phys. Rev. Lett.* **2006**, *97*, 189901.
[19] N. Yazdani, D. Bozyigit, O. Yarema, M. Yarema, V. Wood, *J. Phys. Chem. Lett.* **2014**, *5*, 3522.
[20] M. Liu, O. Voznyy, R. Sabatini, F. P. García De Arquer, R. Munir, A. H. Balawi, X. Lan, F. Fan, G. Walters, A. R. Kirmani, S. Hoogland, F. Laquai, A. Amassian, E. H. Sargent, *Nat. Mater.* **2017**, *16*, 258.
[21] H. Aqoma, S. Y. Jang, *Energy Environ. Sci.* **2018**, *11*, 1603.
[22] S. Lee, M. J. Choi, G. Sharma, M. Biondi, B. Chen, S. W. Baek, A. M. Najarian, M. Vafaie, J. Wicks, L. K. Sagar, S. Hoogland, F. P. de García de Arquer, O. Voznyy, E. H. Sargent, *Nat. Commun.* **2020**, *11*, 4814.
[23] M. J. Choi, Y. J. Kim, H. Lim, E. Alarousu, A. Adhikari, B. S. Shaheen, Y. H. Kim, O. F. Mohammed, E. H. Sargent, J. Y. Kim, Y. S. Jung, *Adv. Mater.* **2019**, *31*, 1805886.
[24] D. Vanmaekelbergh, *Nano Today* **2011**, *6*, 419.
[25] F. Montanarella, J. J. Geuchies, T. Dasgupta, P. T. Prins, C. Van Overbeek, R. Dattani, P. Baesjou, M. Dijkstra, A. V. Petukhov, A. Van Blaaderen, D. Vanmaekelbergh, *Nano Lett.* **2018**, *18*, 3675.
[26] E. Marino, T. E. Kodger, G. H. Wegdam, P. Schall, *Adv. Mater.* **2018**, *30*, 1803433.
[27] Y. Xia, X. Xia, H. C. Peng, *J. Am. Chem. Soc.* **2015**, *137*, 7947.
[28] H. Zhang, J. Yang, T. Hanrath, F. W. Wise, *Phys. Chem. Chem. Phys.* **2014**, *16*, 14640.
[29] H. Choi, J. H. Ko, Y. H. Kim, S. Jeong, *J. Am. Chem. Soc.* **2013**, *135*, 5278.
[30] Y. Kim, F. Che, J. W. Jo, J. Choi, F. P. G. de Arquer, O. Voznyy, B. Sun, J. Kim, M. J. Choi, R. Quintero-Bermudez, F. Fan, C. S. Tan, E. Bladt, G. Walters, A. H. Proppe, C. Zou, H. Yuan, S. Bals, J. Hofkens, M. B. J. Roeffaers, S. Hoogland, E. H. Sargent, *Adv. Mater.* **2019**, *31*, 1805580.
[31] D. Zherebetskyy, Y. Zhang, M. Salmeron, L. W. Wang, *J. Phys. Chem. Lett.* **2015**, *6*, 4711.
[32] S. Ithurria, D. V. Talapin, *J. Am. Chem. Soc.* **2012**, *134*, 18585.
[33] M. Nasilowski, L. Nienhaus, S. N. Bertram, M. G. Bawendi, *Chem. Commun.* **2017**, *53*, 869.
[34] L. K. Sagar, W. Walravens, J. Maes, P. Geiregat, Z. Hens, *J. Phys. Chem. C* **2017**, *121*, 13816.
[35] A. Hazarika, I. Fedin, L. Hong, J. Guo, V. Srivastava, W. Cho, I. Coropceanu, J. Portner, B. T. Diroll, J. P. Philbin, E. Rabani, R. Klie, D. V. Talapin, *J. Am. Chem. Soc.* **2019**, *141*, 13487.
[36] C. R. Bealing, W. J. Baumgardner, J. J. Choi, T. Hanrath, R. G. Hennig, *ACS Nano* **2012**, *6*, 2118.
[37] D. Zherebetskyy, M. Scheele, Y. Zhang, N. Bronstein, C. Thompson, D. Britt, M. Salmeron, P. Alivisatos, L.-W. Wang, *Science* **2014**, *344*, 1380.
[38] J. Endres, D. A. Egger, M. Kulbak, R. A. Kerner, L. Zhao, S. H. Silver, G. Hodes, B. P. Rand, D. Cahen, L. Kronik, A. Kahn, *J. Phys. Chem. Lett.* **2016**, *7*, 2722.
[39] D. Kim, D. H. Kim, J. H. Lee, J. C. Grossman, *Phys. Rev. Lett.* **2013**, *110*, 196802.
[40] L. Ma, D. Qin, Y. Liu, X. Zhan, *J. Mater. Chem. C* **2018**, *6*, 535.
[41] R. H. Gilmore, Y. Liu, W. Shcherbakov-Wu, N. S. Dahod, E. M. Y. Lee, M. C. Weidman, H. Li, J. Jean, V. Bulović, A. P. Willard, J. C. Grossman, W. A. Tisdale, *Matter* **2019**, *1*, 250.
[42] L. Shen, Y. Fang, D. Wang, Y. Bai, Y. Deng, M. Wang, Y. Lu, J. Huang, *Adv. Mater.* **2016**, *28*, 10794.
[43] Y. Liu, M. Gibbs, J. Puthussery, S. Gaik, R. Ihly, H. W. Hillhouse, M. Law, *Nano Lett.* **2010**, *10*, 1960.
[44] O. Schuett, P. Messmer, J. Hutter, J. VandeVondele, in *Electronic Structure Calculations on Graphics Processing Units* (Eds: R. C. Walker, A. W. Götz), Wiley, New York **2016**, p. 173.
[45] U. Borštnik, J. Vandevondele, V. Weber, J. Hutter, *Parallel Comput.* **2014**, *40*, 47.
[46] J. Hutter, M. Iannuzzi, F. Schiffmann, J. Vandevondele, W. Interdiscip, *Wiley Interdiscip. Rev.: Comput. Mol. Sci.* **2014**, *4*, 15.
[47] S. Grimme, J. Antony, S. Ehrlich, H. Krieg, *J. Chem. Phys.* **2010**, *132*, 154104.
[48] J. Vandevondele, M. Krack, F. Mohamed, M. Parrinello, T. Chassaing, J. Hutter, *Comput. Phys. Commun.* **2005**, *167*, 103.
[49] M. Frigo, S. G. Steven, *Proc. IEEE* **2005**, *93*, 216.
[50] J. VandeVondele, J. Hutter, *J. Chem. Phys.* **2003**, *118*, 4365.
[51] J. P. Perdew, K. Burke, M. Ernzerhof, *Phys. Rev. Lett.* **1997**, *78*, 1396.

[52] J. VandeVondele, J. Hutter, *J. Chem. Phys.* **2007**, *127*, 114105.
[53] M. Krack, *Theor. Chem. Acc.* **2005**, *114*, 145.
[54] S. Goedecker, M. Teter, *Phys. Rev. B* **1996**, *54*, 1703.
[55] C. Hartwigsen, S. Goedecker, J. Hutter, *Phys. Rev. B* **1998**, *58*, 3641.
[56] Blender Online Community, *Blender – A 3D Modelling and Rendering Package*, Blender Foundation, Stichting Blender Foundation, Amsterdam, The Netherlands **2018**.
[57] A. H. Larsen, J. J. Mortensen, J. Blomqvist, I. E. Castelli, R. Christensen, M. Dułak, J. Friis, M. N. Groves, B. Hammer, C. Hargus, E. D. Hermes, P. C. Jennings, P. B. Jensen, J. Kermode, J. R. Kitchin, E. L. Kolsbjerg, J. Kubal, K. Kaasbjerg, S. Lysgaard, J. B. Maronsson, T. Maxson, T. Olsen, L. Pastewka, A. Peterson, C. Rostgaard, J. SchiØtz, O. Schütt, M. Strange, K. S. Thygesen, T. Vegge, L. Vilhelmsen, M. Walter, Z. Zeng, K. W. Jacobsen, *J. Phys.: Condens. Matter* **2017**, *29*, 273002.
[58] A. Jain, S. P. Ong, G. Hautier, W. Chen, W. D. Richards, S. Dacek, S. Cholia, D. Gunter, D. Skinner, G. Ceder, K. A. Persson, *APL Mater.* **2013**, *1*, 011002.
[59] Q. Lin, A. Armin, R. C. R. Nagiri, P. L. Burn, P. Meredith, *Nat. Photonics* **2015**, *9*, 106.
[60] J. Zaumseil, H. Sirringhaus, *Chem. Rev.* **2007**, *107*, 1296.
[61] M. J. Speirs, D. N. Dirin, M. Abdu-Aguye, D. M. Balazs, M. V. Kovalenko, M. A. Loi, *Energy Environ. Sci.* **2016**, *9*, 2916.